Novel Fe-Mn-O nanosheets/wood carbon hybrid with tunable surface properties as a superior catalyst for Fenton-like oxidation

Hong Xia[a], Zhen Zhang[a],*, Jia Liu[a], Yang Deng[a], Dongxu Zhang[a], Peiyao Du[a], Shouting Zhang[a], Xiaoquan Lu[a,b],*

[a] *Tianjin Key Laboratory of Molecular Optoelectronic, Department of Chemistry, School of Science, Tianjin University, Tianjin, 300072, China*
[b] *Key Laboratory of Bioelectrochemistry and Environmental Analysis of Gansu Province, College of Chemistry and Chemical Engineering, Northwest Normal University, Lanzhou, 730070, China*

ARTICLE INFO

ABSTRACT

Cost-effective, highly efficient and conveniently recycled heterogeneous catalyst is urgently desirable for wastewater treatment. Wood-derived monolith offers new opportunity because of its toilless functionalization and flexible processing. Herein, ferrum manganese oxide nanosheets (Fe-Mn-O NSs) were successfully grown on the microchannels of carbonized wood to construct a novel 3D wood-derived block for efficient wastewater treatment. The wood carbon not only acts as a 3D substrate to support Fe-Mn-O NSs, but also contributes to unimpeded mass diffusion benefiting from the numerous open channels and hierarchical pores on channel walls. More importantly, except for the exposure of sufficient active sites, several important surface properties (i.e. surface defects, surface charge, low-valence metal concentration and charge transfer) were improved by doping alien-metal element, resulting in greatly improved Fenton activity and stability. Notably, due to flexible processing of wood carbon, this block catalyst can be extended to filter membrane for removing pollutants in flow wastewater.

1. Introduction

Due to rapid population growth and subsequently increased industrial activities, energy and environmental pollution have become global threats for sustainable development of our society [1–3]. Especially, water pollution has risen to one of the most severe issues imperiling human health [4,5]. Unfortunately, the release of contaminants into water, especially organic compounds, is still increasing year by year [6]. Numerous emerging technologies such as biodegradation, physical adsorption, photodegradation, chemical oxidation and nanofiltration have been applied to remove organic compounds [7–12]. However, these methods have suffered from some problems. For instance, biodegradation is susceptible to external influences, and many organics are recalcitrant to be biodegraded. Physical adsorption and membrane filtration undergo sorbent or membrane fouling derived from pollutants adsorption, and can produce excessive amounts of solid wastes [10,13], thus leading to a variety of challenges for sewage treatment. Therefore, there is an urgent demand to develop rapid and effective methods for wastewater treatment.

Advanced oxidation processes (AOPs) have been widely applied as

an environmental-friendly method to remove contaminants [14,15]. Photocatalysis has been researched widely [16,17]. Different photocatalysts, such as MOF supported various semiconductors or different heterojunctions have been developed to improve photocatalytic efficiency [18–22]. However, weak light absorption and poor charge separation limit the applications of photocatalysis. Fenton reaction has garnered tremendous attention due to green nature and complete degradation of organic pollutants by highly active radicals (i.e., $\cdot OH$, $O_2\cdot -$, $^1O_2$, etc) generated from the decomposition of H_2O_2. However, the classical homogeneous Fenton system is limited by several shortcomings such as strict pH requirement (2.5–3.5) and the formation of a mass of iron sludge [23]. In contrast, heterogeneous Fenton or Fenton-like system are more suitable for large-scale applications. Transition metal oxides (Fe, Cu, Co and Mn, etc.) were employed as heterogeneous catalysts for H_2O_2 activation [24–26]. In view of low cost, low toxicity and favorable activity, iron-based materials such as iron hydroxides, iron oxides or iron composite oxides have been researched generally as Fenton catalysts. However, there is still much space for improvement in catalytic performance for these materials by doping, surface modification, morphology control or immobilization on adequate carriers

[24,27–30]. Hetero-metal doping has been verified to be able to affect the Fenton activity by producing more active sites or introducing defects, facilitating the generation of ˙OH in the presence of H_2O_2 [27,31]. Furthermore, the rational design of the morphology is a potential strategy for achieving high catalytic activity. Among the developed nanostructures, 2D nanosheet structure has increased concerns on account of its fascinating physical and chemical properties. In particularly, ultrathin nanosheets can expose sufficient atoms to form effective active sites as well as promote fast interfacial charge transfer [32]. Therefore, the construct of doped or defect-rich ultrathin nanosheets should be an attractive way for significantly improving the catalytic performance of advanced oxidation. However, the synthesis of iron-based nanosheets with ultrathin thickness while simultaneously defect-rich still remains a challenge. Owing to earth abundance, ease of preparation, controllable morphology, particularly in 2D architectures, manganese-based oxides have aroused considerable interests. Nevertheless, limited by the low catalytic activity, the Fenton-like catalytic efficiency of manganese-based oxides is still poor. Utilizing the synergistic effect of materials by hybridization with other high active materials is also an effective strategy to optimize their catalytic performance. Therefore, we surmised that the coupling of manganese oxide nanosheets with iron-based materials might be a promising method to develop superior Fenton catalysts for water treatment.

In addition to high efficiency, low-cost and convenient recycle are also very significant and should not be neglected for practical industrial applications [33]. Wood, an earth-abundant, conveniently engineered material, is recently employed as structural material [13,34]. It opens up a list of energy related applications, such as membrane for gas separation or selective oil/water separation, flow batteries, monolith reactors and so on [34–40]. Nature wood or their derivatives with open microchannels are ideal porous hosts for accommodating active components to fabricate block catalysts for the rapid and convenient recycle of wastewater treatment. What's more, convenient processing of wood and its derivatives can offer more possibilities for membrane filtration. To date, there is few reports about anchoring directly nanosheets in wood or its derivatives as 3D porous material for wastewater treatment.

Herein, for the first time, we developed a 3D wood-derived block catalyst for wastewater treatment by *in situ* forming thin Fe-Mn-O NSs on the open porous microchannels of carbonized wood. The long and irregular channels of wood carbon acted as a 3D substrate to support the Fe-Mn-O hybrid nanosheets. On the other hand, owing to the numerous aligned open channels and hierarchical pores on the channel walls, contaminants in wastewater could get more chances to contact with the anchored Fe-Mn-O NSs in wood carbon channels. More importantly, defect-rich Fe-Mn-O thin nanosheets exposed more catalytic active sites and surface properties of nanosheets could be well tuned via nanocompositing alien-metal ions, resulting in greatly promoted Fenton activity and stability for catalytic oxidation compared with individual MnO_2 NSs/WC and FeOOH/WC, and even outperforming most reported pure Fenton catalysts. A mechanistic insight into the improved catalysis of Fe-Mn-O NSs/WC hybrid was also provided. Furthermore, the catalytic performance under visible light illumination was also investigated. Since this block hybrid could be flexibly processed, the newly developed material was used as a filter membrane for the removal of pollutants in flow waste water sample.

2. Experimental methods

2.1. Preparation of wood carbon (WC)

The bass wood purchased from the Walnut Hollow Company was cut perpendicularly to the growth direction into cubic pieces ($10 \times 20 \times 5$ mm) with a copping saw, and dried at 100 °C overnight to evaporate all the moisture. The dried wood monolith was then transferred into a tube furnace and pretreated at 250 °C for 4 h in air before

further carbonized at 900 °C under flowing nitrogen for 3 h with a heating rate of $3 °C min^{-1}$.

2.2. Preparation of Fe-Mn-O NSs/WC catalysts

First, the as-prepared WC was treated by a mild wet oxidation method using 1.0 M acidic ammonia persulfate solution to obtain a hydrophilic carbon surface [41,42]. Then, 0.158 g $KMnO_4$ and 0.316 g $FeCl_3·6H_2O$ were dissolved into a 100 mL flask with 25 mL of distilled water and the as-treated WC was added into the above solution under uniform stirring. After 90 min, the mixture solution was heated at 120 °C for 4 h under the vigorous stirring. After the reaction solution was cooled down to room temperature, the wood carbon coated with a dark brown product was taken out from the flask, rinsed several times with absolute alcohol and distilled water, and then dried in an oven at 50 °C for overnight. Finally, the as-obtained precursor was heated to 350 °C for 2 h in a muffle furnace with a rate of $10 °C min^{-1}$ to procure Fe-Mn-O NSs/WC hybrids. The Fe-Mn-O NSs/WC with other mass ratios were synthesized similarly through fixed 0.158 g $KMnO_4$ (the mass ratio of $FeCl_3·6H_2O$ to $KMnO_4$ was 0.5, 2 and 4). For comparison, the individual FeOOH/WC and MnO_2 NSs/WC were prepared using the same procedure, where 0.474 g $FeCl_3·6H_2O$ and 0.474 g $KMnO_4$ were added into the starting solution for reaction, respectively. Except otherwise noted, the Fe-Mn-O NSs/WC sample discussed below was synthesized with Fe : Mn raw ratio of 2:1.

2.3. Materials characterization

The crystal structures of the samples were determined by X-ray diffraction (XRD, Cu Ka irradiation, $\lambda = 1.5406$ Å) with a Rigaku SmartLab (9 KW) diffractometer. The morphologies and fine structures of samples were observed by field-emission scanning electron microscope (FE-SEM, Hitachi, SU8010) and transmission electron microscope (TEM, JEM-2100 F with an accelerating voltage of 200 kV). The X-ray photoelectron spectroscopy (XPS) signals were performed on a Thermo Escalab 250xi system with an Al Ka X-ray source (1486.6 eV). The binding energy was calibrated using the C1 s level at 284.6 eV as an internal standard. The surface charge of the various samples was measured with a Malvern Nano-ZS90 zetasizer.

Electrochemical impedance spectroscopy (EIS) was performed on Autolab PGSTAT 302 using a standard three-electrode electrolytic cell with Ag|AgCl as reference electrode and platinum as the counter electrode at room temperature. The working electrode was catalyst-modified FTO glasses. All the Nyquist plots of the different samples were recorded within the frequency range from 10^5 to 0.1 Hz at open-circuit potential in 0.1 M Na_2SO_4 electrolyte solution containing 0.1 M H_2O_2.

Temperature-programmed reduction of H_2 (TPR-H_2) and temperature-programmed desorption of O_2 (TPD-O_2) of samples were conducted in a domestic system using gas chromatography (GC) with thermal conductivity detector (TCD) for monitoring the signals of hydrogen and oxygen [43,44].

2.4. Catalytic tests for Fenton activation

The catalytic performances of different samples were evaluated by activating H_2O_2 toward pollutants degradation. Tetracycline (TC) and various dyes such as methyl orange (MO), methylene blue (MB) and Rhodamine B (RhB) were used as model pollutants. TC was engaged for in-depth kinetics and mechanistic study. The catalytic reaction was performed by putting Fe-Mn-ONSs/WC block into the aqueous solution under the conditions of [TC] $= 20$ mg L^{-1}, [catalyst] $= 3$ mg mL^{-1}, $[H_2O_2] = 0.1$ M. The pH values of solution were adjusted by HCl or NaOH solution (1 M). Before the reaction started, the mixture solution was magnetically stirred for 1 h to obtain an adsorption-desorption equilibrium. Then after a given time interval, quantitative solution was

withdrawn and analyzed the residual concentration of TC using the UV–vis spectroscopy at λ = 357 nm. After each test, tweezers were just used to take the block catalyst to a fresh system for recycle without centrifugation or filtration.

The filtration catalytic performance was evaluated using a home-made cross flow filtration device. The Fe-Mn-ONSs/WC membrane was used as a filter membrane, and the aqueous solution was filtrated through the membrane assisted by vacuum (0.1 MPa). The RhB degradation efficiency was calculated as follows: degradation efficiency (%) = 100 × $(C_0$-$C)/C_0$, where C_0 is the initial MB concentration and C is the MB concentration after filtration.

The active species generated in Fe-Mn/H_2O_2 system were detected by free radicals trapping experiments. Trapping experiments were carried out in a similar experiment device as previously described for the catalytic degradation of TC. Tertbutyl alcohol (TBA, 1 mM), 1,4-benzoquinone (BQ, 1 mM), and furfuryl alcohol (FFA, 5 mM) were chosen as scavengers for hydroxyl radical ($\cdot$OH), superoxide radical ($\cdot O_2$–) and singlet oxygen ($^1O_2$), respectively [27,45,46]. The concentrations of $\cdot$OH and $\cdot O_2$– were quantified by a fluorescence method using coumarin (2 mM) and 4-Chloro-7-nitrobenz-2-oxa-1,3-diazole (NBD-Cl, 0.1 mM) as probes on a Hitachi F7000 fluorescence spectrophotometer [47].

The amount of total iron ions on samples and leached iron ions into the solution were determined by inductively coupled plasma-mass spectrometry (ICP-MS). The ferrous concentration on samples was measured at 510 nm by the iron-phenanthroline complex approach using a UV–vis spectroscopy [48,49].

Degradation products were detected by liquid chromatography-mass spectrometry (LC–MS). It was carried out on an Agilent 6410 triple quadrupole mass spectrometer coupled to an Agilent 1100 series HPLC. Separation was executed on a C18 reverse-phase column. Mobile phase was composed of 80% H_2O containing 0.2% formic acid. The mass spectrometer analysis was performed in positive ionization mode over the range of m/z 100–600 with an electrospray ionization (ESI) source.

3. Results and discussion

To fabricate the 3D Fe-Mn-O NSs/WC composite (Scheme 1), nature wood block (yellow wood) was cut perpendicular to the growth direction of the tree, carbonized, and activated (black wood carbon). The Fe-Mn-O hybrid nanosheets were deposited on the wall of the wood-carbon microchannels via a facile reflux reaction with $KMnO_4$ and $FeCl_3 \cdot 6H_2O$ as starting reagents and wood carbon as supporting materials, then following a low-temperature calcination treatment. The precursor of hybrid nanosheets was first formed by the redox reaction of MnO_4– with wood carbon ($4KMnO_4 + 3C + H_2O = 4MnO_2 + K_2CO_3 + 2KHCO_3$) and the

Scheme 1. Schematic illustration of the synthesis procedure of Fe-Mn-O NSs/WC for water treatment.

hydrolysis reaction of Fe(III). Subsequently, calcination process was conducted in order to achieve appropriate crystallinity and ensure an intimate contact between the nanosheets and wood carbon. After Fe-Mn-O hybrid nanosheets decoration, the wood carbon was changed to redish-brown from black after the reflux reaction and further turned to brown black after calcination (Fig. S1). As a result, Fe-Mn-O NSs/WC with uniform active component loading and superior porous framework was obtained. The aligned and open microchannels derived from wood could significantly facilitate the diffusion of pollutants and gas. Simultaneously, the numerous hierarchical pores on the channel walls could easily trap solution to form continuous diffusion pathways. Pollutants could continuously transport through the open microchannels and were then decomposed by free radicals. Moreover, this unique structure offered more surface areas for Fe-Mn-O NSs to anchor, thereby largely increasing the active sites. With the enhanced mass diffusion and transport as well as well-anchored Fe-Mn-O NSs, the assembled wood-based composite could display greatly improved catalytic performance for water treatment.

The morphology of each step in synthesis process was characterized via SEM and TEM. The SEM measurement revealed that carbonized wood maintained unique anisotropic 3D architecture of wood (Fig. S2). As shown in Fig. 1a, it exhibited a highly porous nature of wood carbon. There were two different long and irregular microchannels in vertically cutting wood carbon. The diameters of the small and large microchannels were typically about 5–15 and 30–70 μm, which stemmed from cellulose fibers and vessels in the raw wood slab, respectively [39,50]. The microstructure of vessel channels in wood carbon was shown in magnified SEM images (Fig. 1b). Numerous vessel pits and horizontally grown spirals along the large wood lumens were observed, which connected the channels together, leading to an enhancement in the amount of water-catalyst interaction as the water passed through the channels. XRD was further carried out to examine the crystalline property of wood carbon (Fig. 1c). The result revealed that an amorphous carbon structure and the peaks at 23.0° and 43.7° could be ascribed to (002) and (101) graphitic planes, respectively [39]. The numerous open microchannels allowed $KMnO_4$ and $FeCl_3 \cdot 6H_2O$ precursor solution to penetrate throughout the entire wood carbon and realize *in situ* uniformly formation of Fe-Mn-O NSs within the 3D carbon matrix. The high-magnification SEM images of the channel in Fe-Mn-O NSs/WC were shown in Fig. 1d–f. As observed, the hybrid nanosheets stood on the walls of the microchannels, and exhibited interconnected thin nanosheets architecture, forming an ordered array with an opened-up network. The most of the nanosheets surface were highly accessible for the solution when used as a catalyst for Fenton oxidation. In addition, for comparison, the morphology of individual MnO_2/WC, FeOOH/WC and Fe-Mn-O NSs/WC with other mass ratios were showed in Fig. S3. The individual FeOOH/WC displayed a spindle-like morphology, but MnO_2/WC showed thin nanosheets architecture. Tuning the raw ratio of Fe/Mn changed the surface morphology with increasing the Fe content. The large nanosheets evolved gradually to smaller ones and then to particle-mixed top layer when the mass ratio of Fe/Mn changed from 0.5:1 to 4:1. Fig. 1g–f revealed the TEM images of Fe-Mn-O NSs, which further confirmed ultrathin nature of Fe-Mn-O hybrid nanosheets. High-resolution TEM (HRTEM) revealed that lattice spacing of 0.256 nm was attributed to (200) plane of birnessite structure [51], which was larger than that of individual MnO_2 nanosheets (0.253 nm, Fig. S4), indicating that Fe had been incorporated into the crystal lattice of MnO_2 forming a hybrid structure. Besides, many distortions and dislocations interspersed among crystal lattices were observed, implying low-crystallinity nature and the formation of a defect-rich structure (Fig. 1i). Undoubtedly, the special defect-rich structure may affect its catalytic performance for H_2O_2 activation. To verify the distribution of each elements, the energy dispersive X-ray (EDX) elemental mapping was characterized. As shown in Figs. 1j and 2, the hybrid nanosheets were composed of Mn, Fe, and O elements, and they were evenly distributed across the nanosheets and the whole block sample.

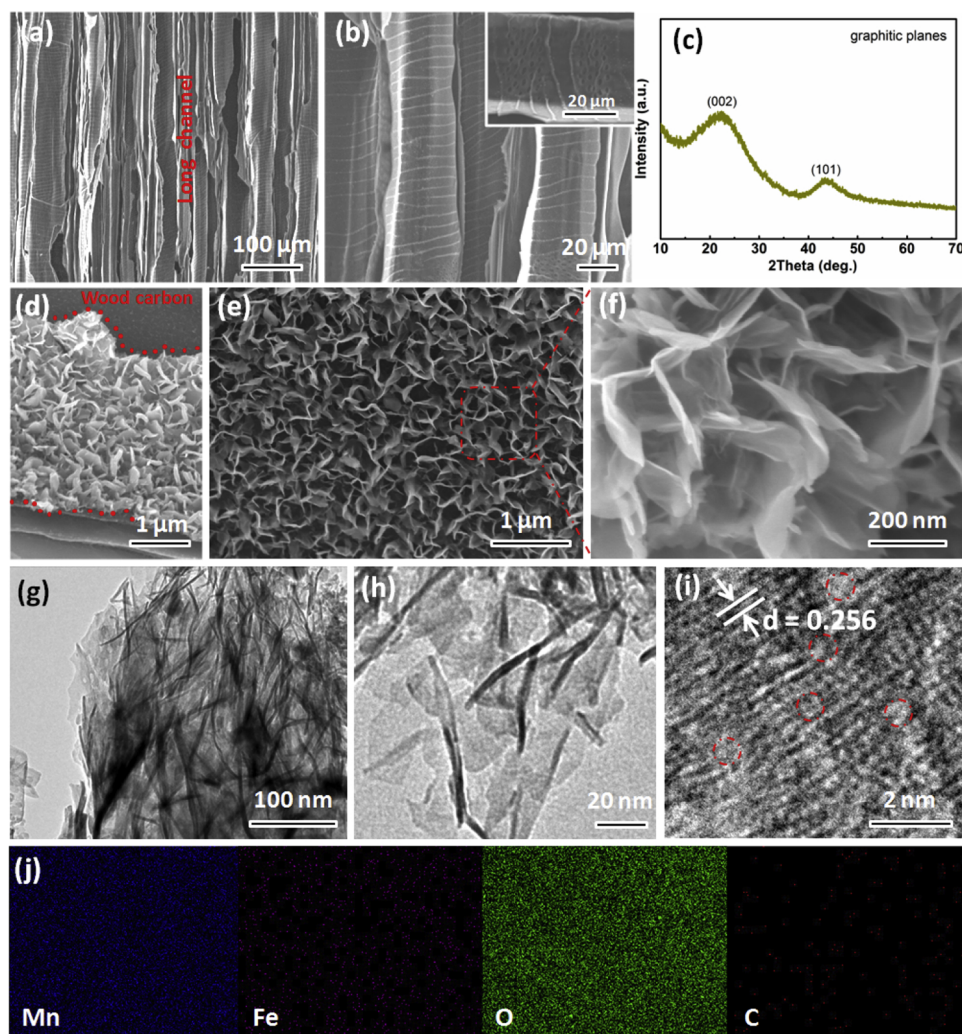The crystal structure of the as-prepared hybrid composites was
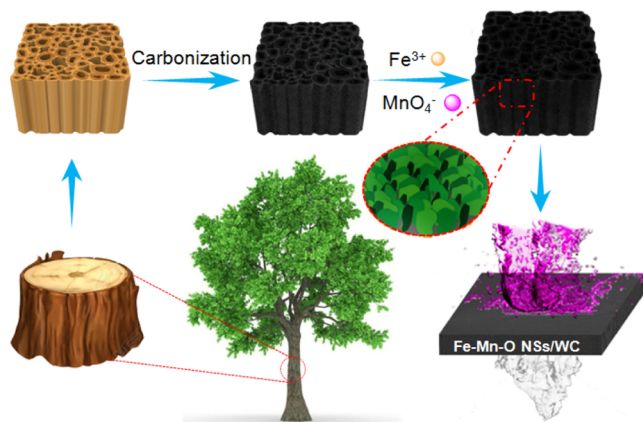
Fig. 1. (a, b) SEM images of wood carbon with long and irregular channels (Inset showed vessel pits and spirals in the channel) (c) XRD of wood carbon, (d–f) SEM images of Fe-Mn-O NSs/WC at different magnifcations. (g–i) TEM and HRTEM images of Fe-Mn-O NSs, and (i) the magnified image of red rectangle area in (h), (j) elemental mapping of the as-synthesized Fe-Mn-O NSs.
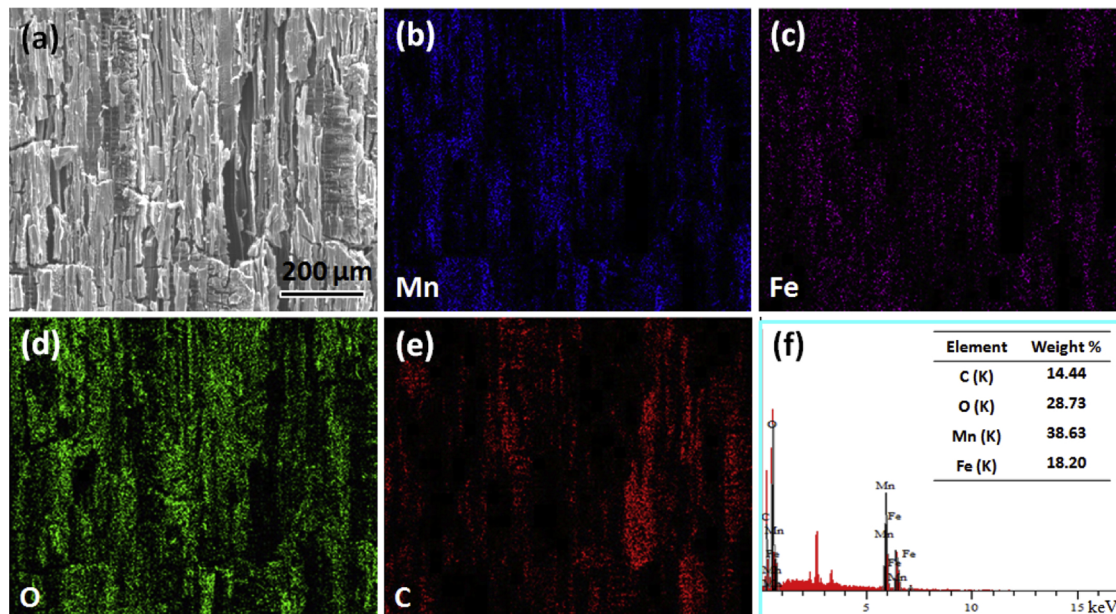

Fig. 2. (a) SEM and elemental mapping spectrum of (b) Mn, (c) Fe, (d) O and (e) C for Fe-Mn-O NSs/WC, (f) corresponding EDX analysis of Fe-Mn-O NSs/WC.
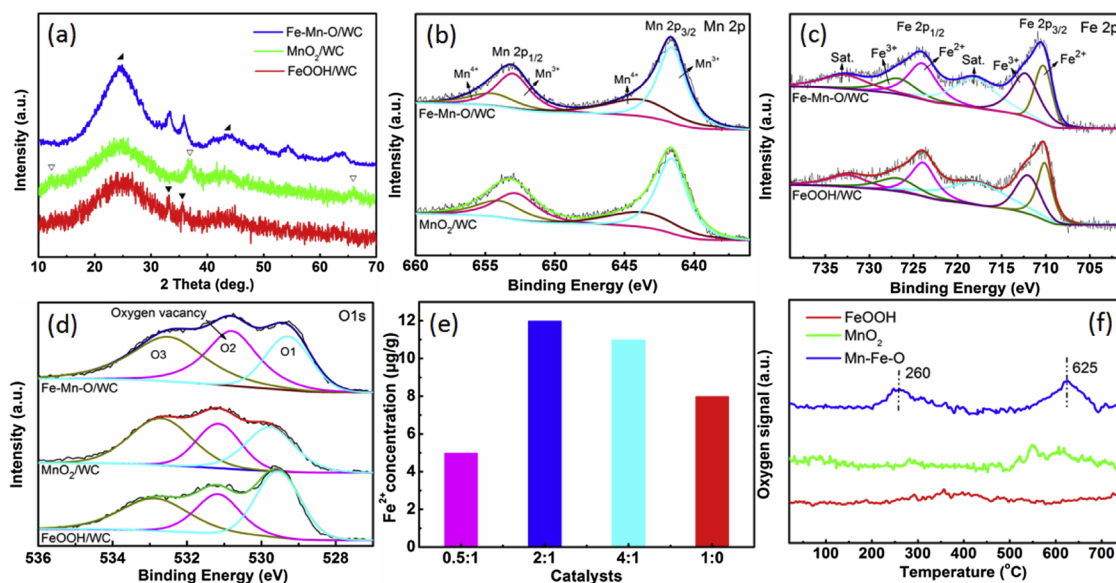
Fig. 3. XRD patterns and XPS analysis of FeOOH/WC, MnO₂NSs/WC and Fe-Mn-ONSs/WC: (a) XRD patterns; (b) high-resolution Mn 2p region for MnO₂NSs/WC and Fe-Mn-O NSs/WC; (c) Fe 2p region for FeOOH/WC and Fe-Mn-O NSs/WC and (d) O 1s region for FeOOH/WC, MnO₂ NSs/WC and Fe-Mn-O NSs/WC, (e) surface Fe^{2+} concentration of different catalysts and (f) O₂-TPD of FeOOH, MnO₂ and Fe-Mn-O hybrid NSs.

confirmed by XRD. As shown in Fig. 3a, the diffraction peaks of sample prepared with only Fe precursor were matched well with the standard orthorhombic phase of FeOOH (JCPDS no. 18-0639). For sample prepared with only Mn precursor, the weak and broad diffraction peaks at 12.3°, 36.6° and 66.1° were attributed to layered birnessite-type MnO₂ (JCPDS no. 80-1098) [51,52]. The hybrid composite (Fe-Mn-O NSs) also displayed birnessite structure. However, it was obvious that the diffraction peaks shifted to lower angle, suggesting an increment in the lattice constant. This observation further confirmed the speculation of the incorporation of iron species into the crystal lattice of MnO₂ because of the relatively larger radius of Fe^{3+} [53]. The FT-IR spectrum also confirmed the existence of Fe−O band (670 cm⁻¹), indicating successfully doping of Fe into MnO₂ nanosheets. Moreover, broad diffraction peaks in XRD explained that the crystallinity was poor, which was also consistent with the TEM analysis. The above results revealed that uniform Fe-Mn-O hybrid nanosheets were successfully grown in wood carbon block, and manganese oxides played a key role in the formation of nanosheets architecture. The surface morphology and active component loading mass can be regulated by changing the raw ratio of Fe/Mn, and the loading mass increased with enlarging the Fe content. Meanwhile, the content of Fe in hybrid nanosheets also increased gradually with adding the starting concentration of Fe salts according to the ICP-MS analysis (Table S1).

Surface properties of hybrid materials such as oxidation states of metallic elements, oxygen vacancies ($V_o^{··}$), interfacial charge transfer, etc were reported to be the key factors to determine their catalytic performance for H₂O₂ activation [27]. Therefore, XPS spectrum was used to analyze the elemental chemical states and confirm the oxygen species, as shown in Fig. 3b–d. For Fe-Mn-O NSs /WC sample, as expected, the full scan spectrum showed the existence of Mn, Fe, O and C elements (Fig. S6). High resolution Mn 2p spectrum showed two characteristic peaks assigned to Mn 2p₃/₂ and Mn 2p₁/₂, respectively. The Mn 2p₃/₂ and 2p₁/₂ peaks could be deconvoluted into two peaks, respectively, including 641.8 eV and 653.6 eV for Mn^{3+}, 643.3 and 654.7 eV for Mn^{4+}, which confirmed the coexistence of Mn^{3+} and Mn^{4+} [51,54]. Furthermore, Mn 3 s spectrum showed two peaks in the range of 79 to 91 eV with BE difference of 4.5 eV, further revealing the existence of Mn^{4+} (Fig. S6). Fig. 3c provided the detailed information of Fe species with corresponding characteristic peaks, deconvoluted by the Fe 2pspectra. As shown in Fig. 3c, Fe species contained Fe^{2+} (710.2

and 723.9 eV), Fe^{3+} (712.1and 726.9 eV), and satellite peaks (717.6 and 730.4 eV) [27,55]. Compared with individual FeOOH/WC, no obvious peak shift was observed but the total concentration of Fe^{3+} and Fe^{2+} on the surface of hybrid composites was increased. Moreover, the relative amount of Fe^{2+} was enlarged on Fe-Mn-O hybrids surface. To further probe the variation of Fe^{2+} content, surface Fe^{2+} on different samples were detected, as displayed in Fig. 3e. Hybrid composites displayed higher surface Fe^{2+} concentration compared to single FeOOH. Fe-Mn-O NSs (2:1) exhibited the highest Fe^{2+} content. Since Fe^{2+}species are the redox sites to activate H₂O₂ for producing free radicals, the high Fe^{2+} concentration in hybrid indicates good Fenton reactivity. For the O 1s spectrums of individual FeOOH/WC, MnO₂ NSs/WC and Fe-Mn-O NSs/WC, three characteristic peaks can be clearly identified. In detail, the peak at 529.2 eV belonged to lattice oxygen (O^{2-}) due to oxygen atoms bound to metals, the peak at 532.5 eV was associated with absorbed oxygen (−OH or O₂), and the peak at 531.2 eV was attributed to defect sites with low oxygen coordination [55,56]. Compared with the single FeOOH, both MnO₂ and Fe-Mn-O hybrid samples showed the incremental absorbed oxygen, which was mainly due to the unique layered structure in favor of the adsorption of water or O₂. The amount of O^{2-} was found to decrease for Fe-Mn-O hybrids due to the generation of more transition metal cations with a lower valence, as unveiled by the Fe 2p spectra and Mn 2p spectra. Furthermore, the area of the peak at 531.2 eV was larger for Fe-Mn-O hybrid than that of single FeOOH or MnO₂, indicating that the as-prepared Fe-Mn-O NSs possessed more oxygen vacancies than the other counterparts. O₂-TPD was conducted to further probe the evolution of oxygen species. As shown in Fig. 3f, over pure FeOOH, the oxygen desorption was not intense, and only oxygen desorption from a few surface monolayers could be observed. Two oxygen desorption peaks were clearly observed on MnO₂ NSs and Fe-Mn-O NSs. The peak at 260 °C was assigned to the desorption of α-oxygen due to the chemisorption of oxygen on the surface oxygen vacancies [27,57]. The peak at higher temperature (625 °C) was ascribed to the desorption of lattice oxygen (β-oxygen) in the bulk [27]. As comparison, the amount of desorbed oxygen was strongly enhanced for Fe-Mn-O NSs sample compared with FeOOH or MnO₂ NSs, which was attributed to the generation of more surface oxygen defects in Fe-Mn-O NSs hybrid. This observation also implied an easier oxygen mobility between the bulk and the surface [51,58]. The reducibility of obtained samples was
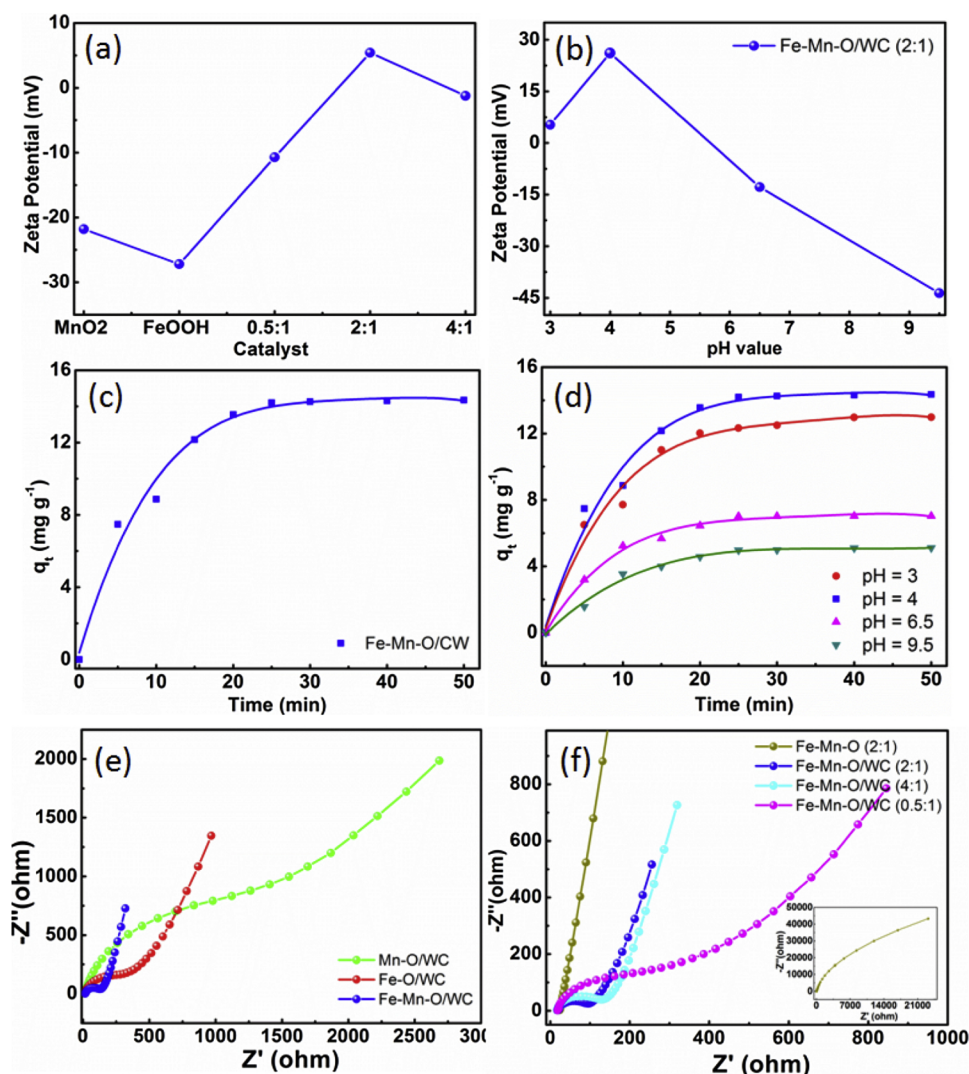
Fig. 4. Zeta potential of (a) different catalysts at pH = 3, (b) Fe-Mn-ONSs/WC at different pH values, (c) TC adsorption on Fe-Mn-O NSs/WC and Fe-Mn-O NSs at pH = 4, (d) TC adsorption on Fe-Mn-O NSs/WC at different pH values in the dark-condition, (e and f) EIS plots of different catalysts measured in 0.1 M Na$_2$SO$_4$ solution containing 0.1 M H$_2$O$_2$. The inset image represented magnified EIS plots of Fe-Mn-O without wood carbon.

demonstrated by H$_2$-TPR in Fig. S7. FeOOH showed two intense reduction peaks at 390 and 502 °C, which was ascribed to the reduction of Fe^{3+} to Fe^{2+} then to Fe [27,44]. MnO$_2$ NSs exhibited two reduction peaks at lower temperatures (297 and 391 °C), corresponding to the reduction of Mn^{4+} to Mn^{3+} and Mn^{3+} to Mn^{2+}, respectively [59]. As for Fe-Mn-O NSs, two much weaker reduction peaks appeared at 370 °C and 461 °C, demonstrating that there was a strong chemical interaction between Fe and Mn in Fe-Mn-O NSs. It may play a vital role in its catalytic activity.

In order to probe the adsorbability toward the pollutants or H$_2$O$_2$, surface charge performance of the obtained catalysts was analyzed by detecting zeta potential. Fe-Mn-ONSs/WC hybrids in a dispersion environment of water exhibited incremental zeta potential compared with FeOOH/WC and MnO$_2$ NSs/WC (Fig. 4a). Fe-Mn-O NSs/WC (2:1) showed the largest zeta potential of 5.5 mV in aqueous solution, which indicated a positively charged surface. As is known, it is beneficial for degradation reaction to develop catalysts with the opposed surface charge to the pollutants because of a better adsorption caused by electrostatic attraction forces [31]. Fe-Mn-ONSs can exhibit a preferable adsorption capacity toward negatively charged pollutants in comparison to single iron oxide or manganic oxide. Fig. 4c showed that the equilibrium TC adsorption capacity of Fe-Mn-ONSs/WC reached 14.50 mg g^{-1}. The effect of solution pH on zeta potential values of Fe-

Mn-O NSs/WC (2:1) was investigated in a pH range of 3–9.5, as shown in Fig. 4b. The zeta potential firstly increased then turned to decrease with creasing the solution pH, whereas there was a threshold value of 26.3 mV at pH = 4.0. In the case of weak acids and bases, Fe-Mn-O NSs/WC hybrids presented a negatively charged surface. In view of employing TC as negatively charged pollutant (Fig. S8), the negative charges on the Fe-Mn-ONSs/WC surface handicapped the adsorption of TC. As illustrated in Fig. 4d, the adsorption capacity of TC decreased from 14.50 mg g^{-1} under pH = 4 to 5.07 mg g^{-1} under pH = 9.5. Fe-Mn-ONSs/WC exhibited the largest adsorption capacity toward TC under pH = 4.0, which implied that pH = 4.0 may be a favorable condition for TC pollutants adsorption, similar to the condition of Fe^{2+}-based AOP. Assuredly, anionic surface defects such as oxygen vacancies were believed to contribute to the enhancement of the surface positive charges of oxides [60]. As for Fe-Mn-O hybrids, there were more surface oxygen defects than that of FeOOH or MnO$_2$ nanosheets verified by the aforementioned XPS and O$_2$-TPD analysis, leading to higher positively charged surface of hybrid. Moreover, it was beneficial for producing more active adsorbed oxygen species (i.e., O–, O$_2$– and O$_2^{2-}$) derived from higher adsorption of oxygen molecules. The zeta potential of Fe-Mn-ONSs/WC (4:1) declined to −0.9 mV, which was due to the increased coverage of FeOOH on the surface of hybrids. The above results suggested that Fe-Mn-ONSs/WC hybrids had superior surface charge
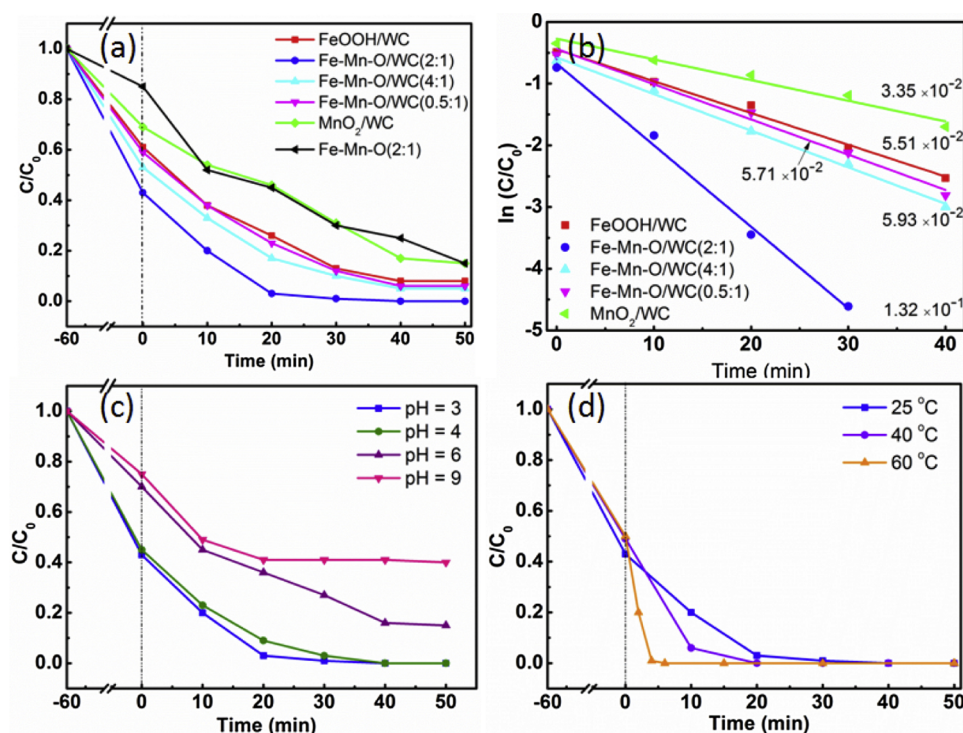
Fig. 5. (a) Catalytic evaluation of catalysts for TC degradation with H_2O_2 at initial pH = 4 at room temperature, (b) corresponding reaction kinetic of TC, the effect of (c) initial pH value and (d) reaction temperature on TC degradation by Fe-Mn-O NSs/WC activated H_2O_2.

due to the formation of oxygen vacancies on the surface, as tuned by fabricating appropriate amount of doping or defect. In addition, the surface positive charges also favored the adsorption of H_2O_2, which could promote effective contact between catalyst and H_2O_2, and also facilitate the catalytic processes in Fenton reactions.

The catalytic activities of the as-obtained Fe-Mn-ONSs/WC with different mass ratios toward Fenton reaction were evaluated by degrading TC with H_2O_2 under pH = 4.0, a favorable condition for the adsorption of TC as confirmed previously (Fig. 4). For comparison, single FeOOH/WC and MnO_2NSs/WC were also tested for control. All the Fenton-like catalytic reactions followed the pseudo-first-order kinetics model ($- \ln(C_t/C_0) = kt$). As shown in Fig. 5a, FeOOH/WC showed a good Fenton catalytic activity of removing 93.0% TC within 40 min, which was superior to those of iron-based catalysts reported elsewhere [25,61]. This was attributed to advantageous porous framework of carrier and sufficient exposure of the active sites owing to high dispersion of FeOOH in wood carbon as proved by small nanoparticles in SEM image (Fig. S3). MnO_2NSs/WC showed a relatively poor activity, whereas enhanced catalytic efficiencies toward TC were observed over Fe-Mn-O NSs/WC with different Fe/Mn mass ratios. Fe-Mn-O NSs/WC (2:1) exhibited the best degradation activity with a rate constant (k) of 1.32×10^{-1} min^{-1}, which was much greater than the values of 3.35×10^{-2} min^{-1} and 5.51×10^{-2} min^{-1} obtained from MnO_2 NSs/WC and FeOOH/WC. This phenomenon indicated the beneficial effect for improving the Fenton reactivity by introducing Fe^{3+} species into MnO_2 nanosheets. Both sufficiently exposed active sites and tuned physicochemical properties of Fe-Mn-O NSs surface had significant impacts on the catalytic performance of Fe-Mn-O NSs/WC in Fenton oxidation. The thin Fe-Mn-O nanosheets possessed large specific surface area, which could lead to sufficient exposure of active sites. Moreover, the nanosheets presented an ordered array with an opened-up network, which ensured their sufficient contact with H_2O_2 and TC in solution (as seen in Fig. 1d–f). In addition, the surface metal ions (Fe and Mn) and surface defects are critical factors to its Fenton activity. On the basis of XPS analysis (Fig. 3b–f), more surface low-valence metal ions were generated in Fe-Mn-O hybrid nanosheets, which could act as

the main active centres to produce $\cdot$OH [25,61]. As displayed in Fig. 3e, surface Fe^{2+} in hybrids showed a "volcano-shaped" diagram with the decreasing of mass ratio of Fe/Mn increases, and Fe-Mn-O NSs/WC (2:1) presented the highest surface concentration of Fe^{2+}, which was consistent with the trend of catalytic activity, implying that surface Fe^{2+} might play a crucial role on Fenton catalysis of Fe-Mn-O NSs/WC. Furthermore, excellent surface charge performance of Fe-Mn-O NSs/WC catalysts (i.e. tunable positively charged surfaces) (Fig. 4a) was beneficial for TC and H_2O_2 adsorption, reinforcing the catalytic oxidation of pollutants. Furthermore, it has been reported that the charge transfer between catalysts and H_2O_2 has a great impact on H_2O_2 activation [27,62]. EIS measurements in 0.1 M Na_2SO_4 solution containing 0.1 M H_2O_2 were carried out to detect the charge transport capacity at the interfaces between various catalysts and H_2O_2. As revealed in Fig. 4e, Fe-Mn-O NSs/WC hybrid exhibited a smaller semicircle diameter than that of single MnO_2 NSs/WC and FeOOH NSs/WC, implying a faster surface reaction rate with better charge transfer of Fe-Mn-O NSs/WC hybrid. Among Fe-Mn-O NSs/WC hybrids with different mass ratios of Fe/Mn, Fe-Mn-O NSs/WC (2:1) exhibited the fastest charge transport ability. Overall, above-mentioned factors were combined to accelerate the Fenton activity of Fe-Mn-O NSs/WC catalyst. As a result, Fe-Mn-O NSs/WC (2:1) showed the optimal degradation rate among all hybrid catalysts (Fig. 5a) based on the merits of highest surface concentration of low-valence metal ions (Fig. 3), the fastest interfacial charge transfer (Fig. 4f) and highest zeta potential with positively charge (Fig. 4a). Simultaneously, strong H_2O_2 adsorption was also contributed to the enhancement in Fenton activity of Fe-Mn-O NSs/WC. In addition, pollutants degradation efficiency of pure Fe-Mn-O NSs was showed in Fig. 5a, which displayed poor degradation rate compared with that of Fe-Mn-O NSs/WC (2:1), indicating the advantage of the porous structure of wood carbon.

The solution pH and temperature have remarkable influences on the catalytic performance of Fenton reaction. Fig. 5c indicated that Fe-Mn-O NSs/WC exhibited excellent Fenton activity at pH below 4.0. The decomposition rate decreased with increasing solution pH. TC degradation was incomplete at pH above 4.0, which might be ascribed to
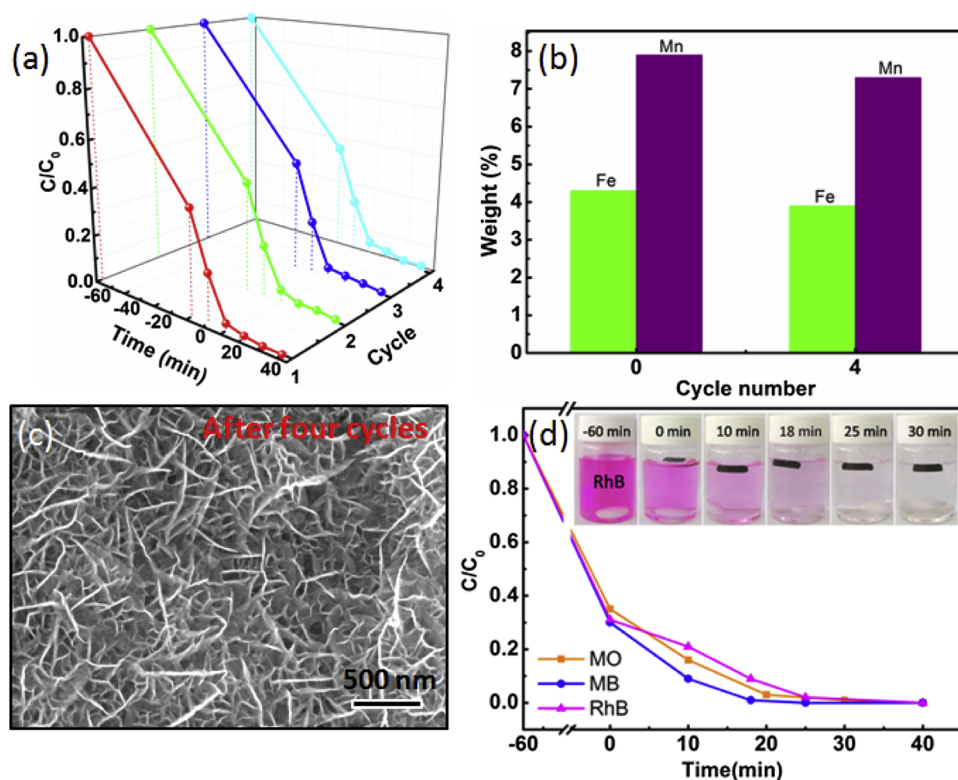
Fig. 6. (a) Stability tests of the catalytic performance using Fe-Mn-O NSs/WC, (b) weight comparison of Fe and Mn for fresh and used Fe-Mn-O NSs/WC catalyst, (c) SEM image of Fe-Mn-O NSs/WC catalyst after four cycles, and (d) different dye pollutants on Fe-Mn-O NSs/WC-H_2O_2 system. The inset showed the corresponding photograph of the color of the remaining RhB solution under different time.

poor TC adsorption for Fe-Mn-O NSs/WC due to lower zeta potential (Fig. 4b). Although degradation was incomplete at high pH values, the decomposition efficiency of TC reached 85.0% within 40 min in neutral environment. It was still preferable to those of the Fenton-like catalysts reported previously [27]. Fig. 5d showed that the decomposition rate of TC increased with the environmental temperature. At 40 °C, the decomposition efficiency of TC reached 94.2% in 10 min. When the temperature was up to 60 °C, only 4 min was needed to achieve the TC decomposition rate of 99.5%, which was far faster than that at 25 °C. In terms of energy consumption, room-temperature adsorption and catalysis are more economic and cost-effective. Fe-Mn-O NSs/WC still had an excellent ability of removing TC in a short time at the ambient temperature. The stability and recyclability of catalysts are two important indicators for practical application. The stability of Fe-Mn-O NSs/WC for AOPs was evaluated by carrying out a test over four cycles. As depicted in Fig. 6a, it maintained almost the same activity level after four cycles. Moreover, the content of Fe and Mn for used Fe-Mn-O NSs/WC catalyst was just slightly lower compared with fresh catalyst, suggesting a low Fe (0.3 wt%) and Mn leaching (0.6 wt%). The SEM image in Fig. 6c depicted that the morphology of catalyst did not change much and still retained interconnected thin nanosheets architecture after four cycles. These indicated that Fe-Mn-O NSs/WC catalyst could maintain an excellent long-term stability. Furthermore, the block structure of Fe-Mn-O NSs/WC made separation from the solution much easier just with tweezers. When a catalytic cycle finished, the bulk catalyst was just taken out by using tweezers, washed and then used into next cycle. Between the two cycles, it was unnecessary to execute tedious centrifugation or filtration processes. In addition, except for TC, Fe-Mn-O NSs/WC hybrid also showed outstanding Fenton activity toward various dyes (i.e. MO, MB, and RhB) under the same measurement conditions (Fig. 6d). The above results indicated that Fe-Mn-O NSs/WC hybrid was a promising Fenton-like catalyst, which exhibited a great suitability for the practical applications of large-scale wastewater treatment due to its high activity, excellent stability, convenient recyclability and easy operation.

Considering the incremental catalytic activity of Fe-Mn-O NSs/WC hybrid for H_2O_2 activation, the mechanism for catalysis was investigated. In general, as Fenton-type catalysts, Fe-Mn-O NSs/WC can catalyze H_2O_2 to generate free radicals such as hydroxyl radical (˙OH), superoxide radical (˙O_2–) etc, which degrade the pollutants by breaking their organic chains. Therefore, the active species involved in the TC degradation were confirmed by adding various radical scavengers when the catalyst reached adsorption equilibrium. As shown in Fig. 7a, TBA exhibited a more remarkable inhibition effect on the catalytic reaction than BQ and FFA, indicating that ˙OH played a dominant role in TC degradation. In the presence of FFA or BQ, TC degradation process was slightly restrained, which revealed that ˙O_2– and $^1O_2$ were involved in this reaction system (Fig. S9). To provide further evidence of production, coumarin and NBD-Cl were used as probes to detect quantitatively the amount of ˙OH and ˙O_2– via photochemistry, respectively [47,49]. Generally, the stronger is the fluorescent signal, the larger is the produced radical amount. The amounts of ˙OH and ˙O_2– radicals for Fe-Mn-O NSs/WC sample were displayed in Fig. 7b and d. It was clear that the amount of ˙OH on Fe-Mn-O NSs/WC increased rapidly with the increase of time, further suggesting that ˙OH was the main active species. As comparison, the intensity of ˙OH on FeOOH/WC and MnO_2 NSs/WC were also analyzed, and the results were shown in Fig. 7c. Obviously, the signal of produced ˙OH on MnO_2 NSs/WC was much weaker relative to the intensity of FeOOH/WC, which demonstrated that the reaction between iron species and H_2O_2 was the major approach for producing ˙OH in this process. Fe-Mn-O NSs/WC showed the largest fluorescence intensity of ˙OH, and it was far larger than that of single FeOOH/WC or MnO_2 NSs/WC, which was well agreed with the degradation experiment. This phenomenon suggested more active sites (surface Fe^{2+} and $V_o^{˙˙}$) on the surface of Fe-Mn-O nanosheets. Fig. 7d witnessed the signal change of ˙O_2– radicals. It displayed that little ˙O_2– was generated at initial stage, and the amount did not increase as the reaction went on. Furthermore, it was reported that surface oxygen vacancies ($V_o^{˙˙}$) could promote the formation of singlet oxygen [27]. The quenching test confirmed the existence of $^1O_2$ in Fe-Mn-O NSs-

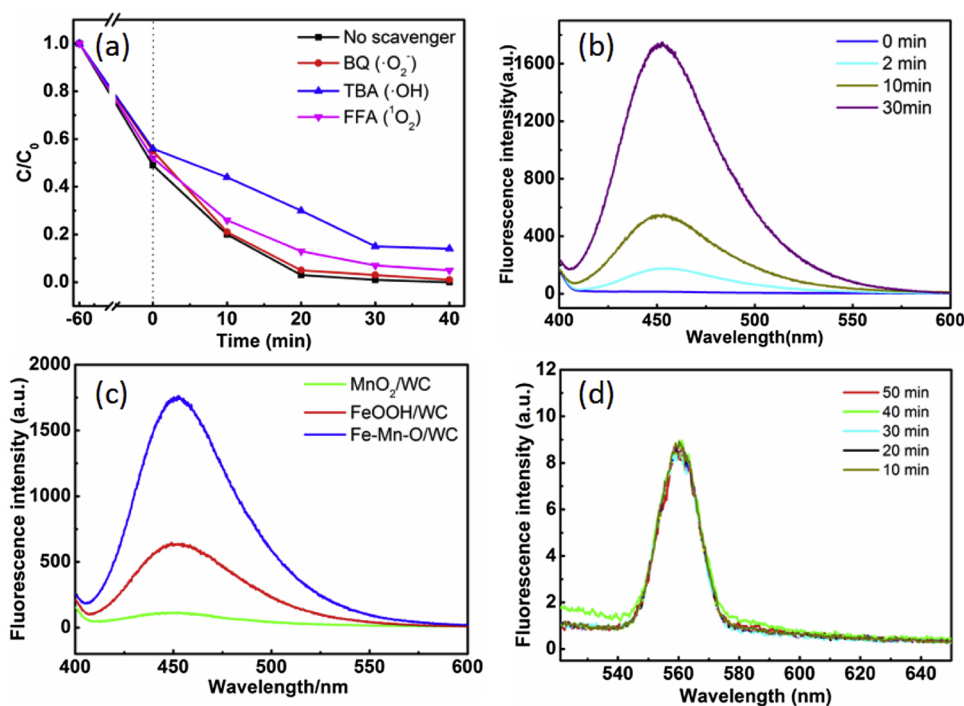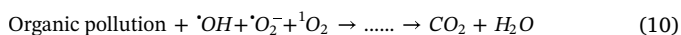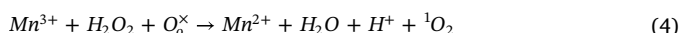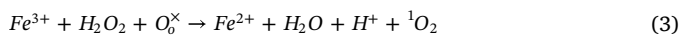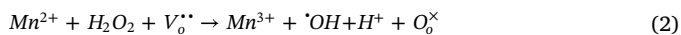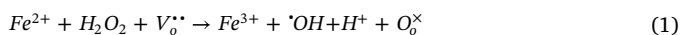**Fig. 7.** (a) Controlled experiments using different radical scavengers (1 mM) for TC degradation, (b and c) $^{\cdot}OH$ radical amount-related fluorescence emission spectra, and (d) $^{\cdot}O_2-$ radical amount-related fluorescence emission spectra.

H_2O_2 system. Therefore, the radical production and decomposition reactions could be expressed by reactions as follows:

$$Fe^{2+} + H_2O_2 + V_o^{\cdot\cdot} \rightarrow Fe^{3+} + {}^{\cdot}OH + H^+ + O_o^{\times} \tag{1}$$

$$Mn^{2+} + H_2O_2 + V_o^{\cdot\cdot} \rightarrow Mn^{3+} + {}^{\cdot}OH + H^+ + O_o^{\times} \tag{2}$$

$$Fe^{3+} + H_2O_2 + O_o^{\times} \rightarrow Fe^{2+} + H_2O + H^+ + {}^1O_2 \tag{3}$$

$$Mn^{3+} + H_2O_2 + O_o^{\times} \rightarrow Mn^{2+} + H_2O + H^+ + {}^1O_2 \tag{4}$$

$${}^{\cdot}OH + H_2O_2 \leftrightarrow HO_2^{\cdot} + H_2O \tag{5}$$

$$2HO_2^{\cdot} \rightarrow {}^1O_2 + H_2O^2 \tag{6}$$

$$HO_2^{\cdot} \leftrightarrow {}^{\cdot}O_2^- + H^+ \tag{7}$$

$$HO_2^{\cdot} + {}^{\cdot}o_2^- \rightarrow {}^1O_2 + HO_2^- \tag{8}$$

$${}^{\cdot}O_2^- + {}^{\cdot}OH \rightarrow {}^1O_2 + OH^- \tag{9}$$

$$\text{Organic pollution} + {}^{\cdot}OH + {}^{\cdot}O_2^- + {}^1O_2 \rightarrow \ldots\ldots \rightarrow CO_2 + H_2O \tag{10}$$

Except for the pure Fenton reaction, the catalytic performance of Fe-Mn-O/WC under visible light irradiation in the presence of H_2O_2 was shown in Fig. 8(a). With only light irradiation, only 15% of TC was degraded in 40 min, suggesting weak direct photolysis of TC (Fig. S10). When in the presence of Fe-Mn-O/WC, TC could be completely degraded in 15 min, which showed a faster degradation rate compared with pure Fenton reaction. Moreover, it exhibited better photo-degradation efficiency than pure FeOOH/WC or MnO$_2$/WC. Fig. 8b showed the PL emission spectra of MnO$_2$/WC and Fe-Mn-O/WC. It was found that the emission position was not much changed after doping Fe, but the emission intensity significantly decreased. This indicated better charge separation for Fe-Mn-O/WC hybrid. The emission lifetime was recorded by time-resolved PL decay spectra over MnO$_2$/WC, FeOOH/WC and Fe-Mn-O/WC hybrid (Fig. 8c). Electron average lifetime (τ_{av}) was also calculated, which was listed in Table S2. The average lifetime of photo-excited charge for Fe-Mn-O/WC hybrid was 5.20 ns, which was longer than that of MnO$_2$/WC (5.01 ns) and FeOOH/WC (1.59 ns),

indicating more efficient charge separation. Moreover, the electrons with long lifetime are also benefit for the reduction of Fe(III). Furthermore, the thinner nanosheets and larger specific surface area with exposure of more active sites were also partially factors to the enhanced activity of Fe-Mn-O/WC compared with MnO$_2$ nanosheets and spindle-shaped FeOOH (Fig. S3). After photo-degradation process, the composition and structure of Fe-Mn-O/WC were preserved, which indicated good stability under light irradiation (Fig. S11). To probe the mechanism of photocatalysis, trapping experiments were carried out, as shown in Fig. 8d. It was obvious that TC degradation process was markedly restrained in the presence of TBA, revealing that $^{\cdot}OH$ played an important role in TC photo-degradation. BQ exhibited an ignorable inhibition effect, which indicated that $^{\cdot}O_2-$ had almost no effects on photocatalysis process. The amount of $^{\cdot}OH$ production decreased as the pH of the solution increased (Fig. S12). This might be due to two main reasons, on the one hand, Fe-Mn-O NSs/WC presented a negatively charged surface in the case of weak acids and bases (Fig. 4b), which was unfavorable for the adsorption of H_2O_2, on the other hand, it was easier to form Fe(OH)$_3$ at high pH, which would lead to the decrease in the activation of H_2O_2. Due to $^{\cdot}O_2-$ derived from the decomposition of H_2O_2, the amount of $^{\cdot}O_2-$ would decrease with the decreasing of $^{\cdot}OH$ production. To further understand the degradation process, Mott-Schottky plot of Fe-Mn-O/WC was measured in dark condition (Fig. 8e). It was worth noting that Fe doped MnO$_2$ nanosheet was identified as n-type semiconductor due to the positive slope in the Mott-Schottky plot. The flat band (V_{fb}) was determined to be 0.43 V (vs Ag/AgCl). In general, for n-type semiconductors, the conduction band potential is nearly equal to the flat-band potential. Thus, the conduction band potential of Fe-Mn-O nanosheets was 0.43 V, which was more positive than that of $O_2/^{\cdot}O_2^-$ potential (-0.33 eV). The photo-generated electrons could not reduce the adsorbed O_2 to produce $^{\cdot}O_2^-$, which was consistent with the results of trapping experiments. Considering that the holes in Fe-Mn-O/WC were not apt to oxidize H_2O or OH- into $\cdot$OH, the whole catalytic process was illustrated in Fig. 8f.

In addition, degradation products were identified by LC–MS. Some intermediates were detected, which were listed in Table S3. Based on the analysis of mass spectrum, the TC degradation pathways under
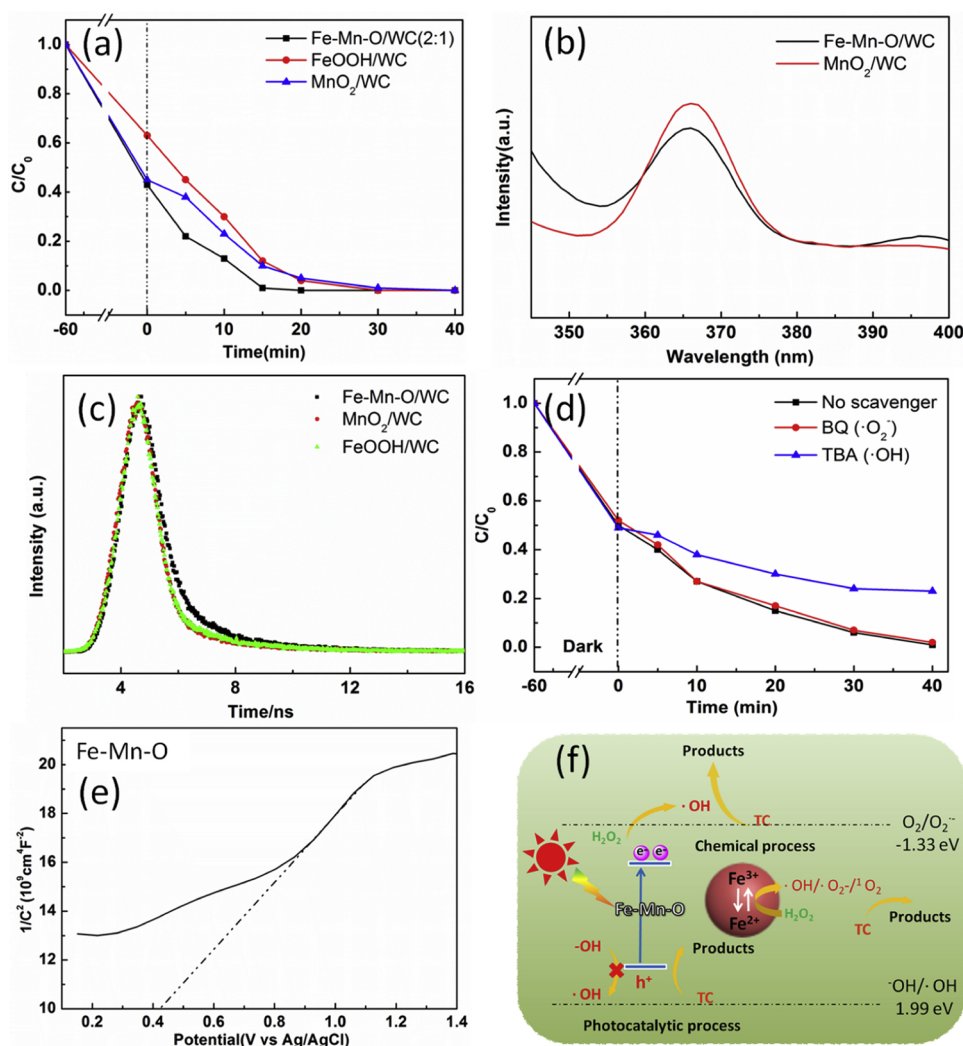
Fig. 8. (a) Photo-Fenton degradation of TC; (b) PL emission spectra (the excitation wavelength is 325 nm); (c) time-resolved PL decay curves of Fe-Mn-O/WC, MnO$_2$/WC and FeOOH/WC; (d) controlled experiments using different radical scavengers (1 mM) for TC degradation; (e) Mott-Schottky plots of the Fe-Mn-O measured in 0.1 M Na$_2$SO$_4$ solution and (f) schematic illustration of catalytic mechanism of Fe-Mn-O/WC in H$_2$O$_2$/visible light system.

visible light radiation were proposed, as presented in Fig. S13. Intermediates with m/z of 432.12 (P1) and 416.12 (P2) were assigned as the dealkylation products of TC. Products with m/z 375.10 (P3), 278.12 (P4), 241.13 (P5), and 120.01 (P6) were assumed as the further oxidation products. These ring-opening products were finally oxidized into CO$_2$ and H$_2$O.

To test the wastewater processing efficiency of the 3D Fe-Mn-O NSs/WC membrane, MB removal tests were carried out. Fig. 9a depicted the testing device for the degradation of MB and the color change as the solution flowed through the Fe-Mn-O NSs/WC membrane. The degradation ability was quantitatively confirmed by UV–vis measurements (Fig. 9b). The Fe-Mn-O NSs/WC membrane showed remarkable performance for MB removal with an efficiency of ca. 99.8%. Moreover, the Fe-Mn-O NSs/WC membrane showed outstanding MB removal activity over a wide range of MB concentrations. Above 90% of the degradation efficiency was maintained for all concentrations up to 30 mg L^{-1} (Fig. 9d). The Fe-Mn-O NSs/WC membrane also exhibited high removal efficiency (97%) when the solution flowed through the wood carbon membrane using a home-made cross flow filtration device (Fig. 9e). The fast and efficient removal of MB by the developed Fe-Mn-O NSs/WC membrane can be attributed to two reasons. First, the uniform Fe-Mn-O NSs throughout the channels of wood carbon served as efficient active sites for the catalytic process to take place. Next, the

hierarchical, open channels and the perforation plates within the wood carbon membrane led to close and effective contact between the Fe-Mn-O NSs/WC and MB solution, which enabled a highly efficient degradation of MB (Fig. 9f). Notably, the unique mesoporous structure of wood carbon can induce superior fluid dynamics as water passed through the 3D membrane. Fig. 9f illustrated the 3D microstructure of the Fe-Mn-O NSs/WC membrane. In addition to the long channels and perforation plates, many vessel pits were observed in the channels, which indicated that wastewater flowed through the pits in a more complex manner. Under such circumstance, diffusion must take place instead of free liquid advection for a fluid to flow to other adjacent channels [13]. Numerous irregular vessels are weaved to form a 3D network, which commands transport in longitudinal, radial, and tangential three directions, triggering a dual effect of reduced flow rate (enhanced residence time for the pollutants) and augmented surface area for pollutants diffusion. All these factors ultimately ensured that augmented pollutants removal occurred throughout the entire wood carbon block owing to the intrinsic mesostructure originated from the wood. Besides, the photograph and SEM image of Fe-Mn-O NSs/WC after treatment were shown in Fig. S14. It showed that the structure of the catalyst membrane and Fe-Mn-O NSs were maintained, which further confirmed the stability of the catalyst.
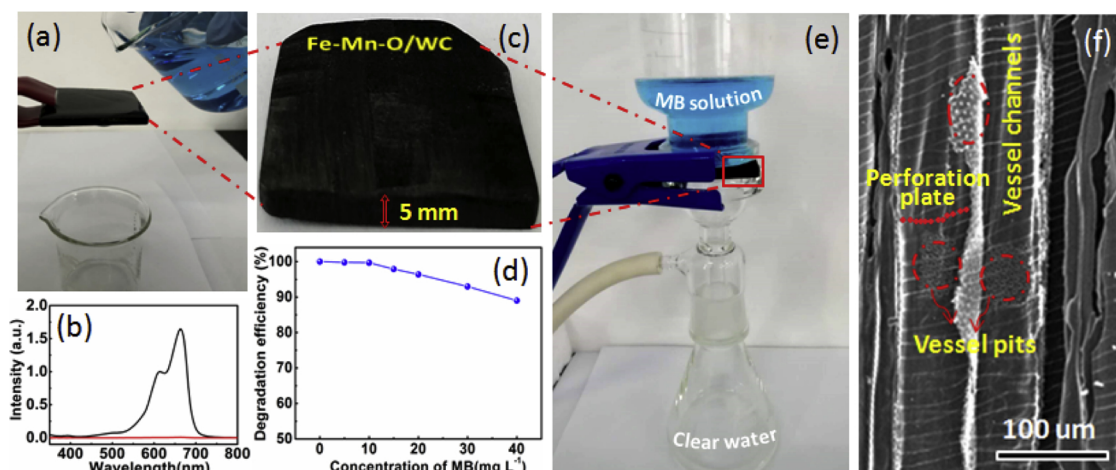
Fig. 9. (a) Demonstration of water treatment using a Fe-Mn-O NSs/WC membrane, the blue solution in beaker consisted of an aqueous mixture of MB (10 mg L^{-1}) and H$_2$O$_2$ (0.1 M); (b) UV–vis measurements of the MB solution before (in black) and after (in red) flowing through Fe-Mn-O NSs/WC membrane; (c) Zoom-in of the black Fe-Mn-O NSs/WC membrane. The membrane dimensions are 50 mm × 50 mm × 5 mm; (d) the degradation efficiency at different concentrations of the MB solution; (e) digital photograph of the home-made filtration device for MB degradation; (f) SEM image of the long wood channels with vessels and perforation plates.

4. Conclusion

In this work, we demonstrated that a 3D mesoporous wood-derived composite decorated with thin Fe-Mn-O hybrid nanosheets could serve as a superior catalyst for wastewater treatment, which was ascribed to the synergistic effect of uniformly distributed Fe-Mn-O nanosheets and the channel structure of carbonized wood. Benefiting from the numerous aligned open channels and the hierarchical pores on the channel walls, catalysts could get more opportunities to contact H$_2$O$_2$ and pollutants in solution, leading to effective activation of H$_2$O$_2$ to degrade pollutants. Meanwhile, thin Fe-Mn-O nanosheets with large specific surface area can expose adequately active sites. More importantly, several important surface properties such as surface defects, low-valence metal ions concentration and interfacial charge transfer were improved by doping alien-metal element, which facilitated both Fenton activity and stability of Fe-Mn-O NSs/WC. The catalytic performance was further improved when light illumination was introduced into the system. The block hybrid can be recycled easily by using tweezers. Because of flexible processing, this block hybrid can be employed as filter membrane for removing pollutants in flow wastewater sample.

Declaration of Competing Interest

The authors declare no conflict of interest.

Appendix A. Supplementary data

Supplementary material related to this article can be found, in the online version, at doi:https://doi.org/10.1016/j.apcatb.2019.118058.

References

[1] Y.F. Zhang, S.J. Park, Facile construction of MoO$_3$@ZIF-8 core-shell nanorods for efficient photoreduction of aqueous Cr (VI), Appl. Catal. B: Environ. 240 (2019) 92–101, https://doi.org/10.1016/j.apcatb.2018.08.077.
[2] Z. Wang, C. Li, K. Domen, Recent developments in heterogeneous photocatalysts for solar-driven overall water splitting, Chem. Soc. Rev. 48 (2019) 2109–2125, https://doi.org/10.1039/c8cs00542g.
[3] Y.F. Zhang, S.J. Park, Formation of hollow MoO$_3$/SnS$_2$ heterostructured nanotubes for efficient light-driven hydrogen peroxide production, J. Mater. Chem. A 6 (2018) 20304–20312, https://doi.org/10.1039/c8ta08385a.
[4] K. Dashtian, M. Ghaedi, S. Hajati, Photo-sensitive Pb$_5$S$_2$I$_6$ crystal incorporated polydopamine biointerface coated on nanoporous TiO$_2$ as an efficient signal-on photoelectrochemical bioassay for ultrasensitive detection of Cr(VI) ions, Biosens. Bioelectron. 132 (2019) 105–114, https://doi.org/10.1016/j.bios.2019.02.042.
[5] Y.F. Zhang, S.J. Park, Stabilization of dispersed CuPd bimetallic alloy nanoparticles on ZIF-8 for photoreduction of Cr(VI) in aqueous solution, Chem. Eng. J. 369 (2019) 353–362, https://doi.org/10.1016/j.cej.2019.03.083.
[6] P.V. Nidheesh, R. Gandhimathi, S.T. Ramesh, Degradation of dyes from aqueous solution by Fenton processes: a review, Environ. Sci. Pollut. Res. 20 (2013) 2099–2132, https://doi.org/10.1007/s11356-012-1385-z.
[7] I. Ali, New generation adsorbents for water treatment, Chem. Rev. 112 (2012) 5073–5091, https://doi.org/10.1021/cr300133d.
[8] L. Huang, J. Chen, T. Gao, M. Zhang, Y. Li, L. Dai, L. Qu, G. Shi, Reduced graphene oxide membranes for ultrafast organic solvent nanofiltration, Adv. Mater. 28 (2016) 8669–8674, https://doi.org/10.1002/adma.201601606.
[9] M. Xing, W. Xu, C. Dong, Y. Bai, J. Zeng, Y. Zhou, J. Zhang, Y. Yin, Metal sulfides as excellent co-catalysts for H$_2$O$_2$ decomposition in advanced oxidation processes, Chemistry 4 (2018) 1359, https://doi.org/10.1016/j.chempr.2018.03.002.
[10] Y. Lv, C. Zhang, A. He, S.J. Yang, G.P. Wu, S.B. Darling, Z.K. Xu, Photocatalytic nanofiltration membranes with self-cleaning property for wastewater treatment, Adv. Funct. Mater. 27 (2017) 1700251, , https://doi.org/10.1002/adfm.201700251.
[11] S. Mosleh, M.R. Rahimi, M. Ghaedi, K. Dashtian, S. Hajati, Sonochemical-assisted synthesis of CuO/Cu$_2$O/Cu nanoparticles as efficient photocatalyst for simultaneous degradation of pollutant dyes in rotating packed bed reactor: LED illumination and central composite design optimization, Ultrason. Sonochem. 40 (2018) 601–610, https://doi.org/10.1016/j.ultsonch.2017.08.007.
[12] M.H. Barzegar, M. Ghaedi, V.M. Avargani, M.M. Sabzehmeidani, F. Sadeghfar, R. Jannesar, Electrochemical synthesis of Zn:ZnO/Ni$_2$P and efficient photocatalytic degradation of Auramine O in aqueous solution under multi-variable experimental design optimization, Polyhedron 165 (2019) 1–8, https://doi.org/10.1016/j.poly.2019.02.003.
[13] F. Chen, A.S. Gong, M. Zhu, G. Chen, S.D. Lacey, F. Jiang, Y. Li, Y. Wang, J. Dai, Y. Yao, J. Song, B. Liu, K. Fu, S. Das, L. Hu, Mesoporous, three-dimensional wood membrane decorated with nanoparticles for highly efficient water treatment, ACS Nano 11 (2017) 4275–4282, https://doi.org/10.1021/acsnano.7b01350.
[14] E. Brillas, I. Sirés, M.A. Oturan, Electro-Fenton process and related electrochemical technologies based on Fenton's reaction chemistry, Chem. Rev. 109 (2009) 6570–6631, https://doi.org/10.1021/cr900136g.
[15] H. Xia, Z. Zhang, J. Liu, X. Ning, S. Zhang, X. Lu, Developing superior catalysts engineered by multichannel healing strategy for advanced oxidation, Appl. Catal. B: Environ. 250 (2019) 189–199, https://doi.org/10.1016/j.apcatb.2019.03.033.
[16] M.M. Sabzehmeidani, H. Karimi, M. Ghaedi, Sonophotocatalytic treatment of rhodamine B using visible-light-driven CeO$_2$/Ag$_2$CrO$_4$composite in a batch mode based on ribbon-like CeO$_2$ nanofibers via electrospinning, Environ. Sci. Pollut. Res. 26 (2019) 8050–8068, https://doi.org/10.1007/s11356-019-04253-8.
[17] S.E. Mousavinia, S. Hajati, M. Ghaedi, K. Dashtian, Novel nanorose-like Ce(III)-doped and undoped Cu(II)–biphenyl-4,4-dicarboxylic acid (Cu(II)–BPDCA) MOSs as visible light photocatalysts: synthesis, characterization, photodegradation of toxic dyes and optimization, Phys. Chem. Chem. Phys. 18 (2016) 11278–11287, https://doi.org/10.1039/c6cp00910g.
[18] S. Mosleh, M.R. Rahimi, M. Ghaedi, K. Dashtian, Sonophotocatalytic degradation of trypan blue and vesuvine dyes in the presence of blue light active photocatalyst of

Ag$_3$PO$_4$/Bi$_2$S$_3$-HKUST-1-MOF: central composite optimization and synergistic effect study, Ultrason. Sonochem. 32 (2016) 387–397, https://doi.org/10.1016/j.ultsonch.2016.04.007.

[19] S. Mosleh, M.R. Rahimi, M. Ghaedi, K. Dashtianb, S. Hajati, Photocatalytic degradation of binary mixture of toxic dyes by HKUST-1 MOF and HKUST-1-SBA-15 in a rotating packed bed reactor under blue LED illumination: central composite design optimization, RSC Adv. 6 (2016) 17204–17214, https://doi.org/10.1039/c5ra24564h.

[20] S. Mosleh, M.R. Rahimi, M. Ghaedi, K. Dashtian, S. Hajati, BiPO$_4$/Bi$_2$S$_3$-HKUST-1-MOF as a novel blue light-driven photocatalyst for simultaneous degradation of toluidine blue and auramine-O dyes in a new rotating packed bed reactor: optimization and comparison to a conventional reactor, RSC Adv. 6 (2016) 63667–63680, https://doi.org/10.1039/c6ra10385e.

[21] K. Dashtian, M. Ghaedia, H. Shirinzadeh, S. Hajati, S. Shahbazi, Achieving enhanced blue-light-driven photocatalysis using nanosword-like VO$_2$/CuWO$_4$ type II n-n heterojunction, Chem. Eng. J. 339 (2018) 189–203, https://doi.org/10.1016/j.cej.2018.01.107.

[22] M. Amiri, K. Dashtian, M. Ghaedi, S. Mosleh, R. Jannesar, Bi$_2$WO$_6$/Ag$_3$PO$_4$–Ag Z-scheme heterojunction as a new plasmonic visible-light-driven photocatalyst: performance evaluation and mechanism study, New J. Chem. 43 (2019) 1275–1284, https://doi.org/10.1039/c8nj05195j.

[23] X. Qian, Y. Wu, M. Kan, M. Fang, D. Yue, J. Zeng, Y. Zhao, FeOOH quantum dots coupled g-C$_3$N$_4$ for visible light driving photo-Fenton degradation of organic pollutants, Appl. Catal. B: Environ. 237 (2018) 513–520, https://doi.org/10.1016/j.apcatb.2018.05.074.

[24] L. Guo, F. Chen, X. Fan, W. Cai, J. Zhang, S-doped α-Fe$_2$O$_3$ as a highly active heterogeneous Fenton-like catalyst towards the degradation of acid orange 7 and phenol, Appl. Catal. B: Environ. 96 (2010) 162–168, https://doi.org/10.1016/j.apcatb.2010.02.015.

[25] S. Karthikeyan, M.P. Pachamuthu, M.A. Isaacs, S. Kumar, A.F. Lee, G. Sekaran, Cu and Fe oxides dispersed on SBA-15: A Fenton type bimetallic catalyst for N, N-diethyl-p-phenyl diamine degradation, Appl. Catal. B: Environ. 199 (2016) 323–330, https://doi.org/10.1016/j.apcatb.2016.06.040.

[26] H. Gao, H. Yang, J. Xu, S. Zhang, J. Li, Photoactuation healing of FeOOH@g-C$_3$N$_4$ catalyst for efficient and stable activation of persulfate, Small (2018) 1801353, https://doi.org/10.1002/smll.201702225.

[27] J. Li, J. Miao, X. Duan, J. Dai, Q. Liu, S. Wang, W. Zhou, Z. Shao, Fine-tuning surface properties of perovskites via nanocompositing with inert oxide toward developing superior catalysts for advanced oxidation, Adv. Funct. Mater. 28 (2018) 1804654, , https://doi.org/10.1002/adfm.201804654.

[28] J. Du, J. Bao, X. Fu, C. Lu, S.H. Kim, Mesoporous sulfur-modified iron oxide as an effective Fenton-like catalyst for degradation of bisphenol A, Appl. Catal. B: Environ. 184 (2016) 132–141, https://doi.org/10.1016/j.apcatb.2015.11.015.

[29] Y. Liu, Z. Chen, C.H. Shek, C.M.L. Wu, J.K.L. Lai, Hierarchical mesoporous MnO$_2$ superstructures synthesized by soft-interface method and their catalytic performances, ACS Appl. Mater. Interfaces 6 (2014) 9776–9784, https://doi.org/10.1021/am502191k.

[30] J. Wang, C. Liu, J. Li, R. Luo, X. Hu, X. Sun, J. Shen, W. Han, L. Wang, In-situ incorporation of iron-copper bimetallic particles in electrospun carbon nanofibers as an efficient Fenton catalyst, Appl. Catal. B: Environ. 207 (2017) 316–325, https://doi.org/10.1016/j.apcatb.2015.11.015.

[31] M.L. Tummino, E. Laurenti, F. Deganello, A.B. Prevot, G. Magnacca, Revisiting the catalytic activity of a doped SrFeO$_3$ for water pollutants removal: effect of light and temperature, Appl. Catal. B: Environ. 207 (2017) 174–181, https://doi.org/10.1016/j.apcatb.2017.02.007.

[32] J. Huang, J. Chen, T. Yao, J. He, S. Jiang, Z. Sun, Q. Liu, W. Cheng, F. Hu, Y. Jiang, Z. Pan, S. Wei, CoOOH nanosheets with high mass activity for water oxidation, Angew. Chem. Int. Ed. 54 (2015) 8722–8727, https://doi.org/10.1002/anie.201502836.

[33] Y. Fan, W. Ma, D. Han, S. Gan, X. Dong, L. Niu, Convenient recycling of 3D AgX/graphene aerogels (X = Br, Cl) for efficient photocatalytic degradation of water pollutants, Adv. Mater. 27 (2015) 3767–3773, https://doi.org/10.1002/adma.201500391.

[34] Q. Fu, F. Ansari, Q. Zhou, L.A. Berglund, Wood nanotechnology for strong, mesoporous, and hydrophobic biocomposites for selective separation of oil/water mixtures, ACS Nano 12 (2018) 2222–2230, https://doi.org/10.1021/acsnano.8b00005.

[35] Y. Huang, Y. Chen, X. Fan, N. Luo, S. Zhou, S.C. Chen, N. Zhao, C.P. Wong, Wood derived composites for high sensitivity and wide linear-range pressure sensing, Small 14 (2018) 1801520, , https://doi.org/10.1002/smll.201801520.

[36] Y. Liu, Y. Su, J. Guan, J. Cao, R. Zhang, M. He, K. Gao, L. Zhou, Z. Jiang, 2D heterostructure membranes with sunlight-driven self-cleaning ability for highly efficient oil-water separation, Adv. Funct. Mater. 28 (2018) 1706545, https://doi.org/10.1002/adfm.201706545.

[37] Y. Wang, G. Sun, J. Dai, G. Chen, J. Morgenstern, Y. Wang, S. Kang, M. Zhu, S. Das, L. Cui, L. Hu, A high-performance, low-tortuosity wood-carbon monolith reactor, Adv. Mater. 29 (2017) 1604257, , https://doi.org/10.1002/adma.201604257.

[38] T. Li, H. Liu, X. Zhao, G. Chen, J. Dai, G. Pastel, C. Jia, C. Chen, E. Hitz, D. Siddhartha, R. Yang, L. Hu, Scalable and highly efficient mesoporous wood-based solar steam generation device: localized heat, rapid water transport, Adv. Funct. Mater. 28 (2018) 1707134, , https://doi.org/10.1002/adfm.201707134.

[39] F. Shen, W. Luo, J. Dai, Y. Yao, M. Zhu, E. Hitz, Y. Tang, Y. Chen, V.L. Sprenkle, X. Li, L. Hu, Ultra-thick, low-tortuosity, and mesoporous wood carbon anode for high-performance sodium-ion batteries, Adv. Energy Mater. 6 (2016) 1600377, , https://doi.org/10.1002/aenm.201600377.

[40] H. Song, S. Xu, Y. Li, J. Dai, A. Gong, M. Zhu, C. Zhu, C. Chen, Y. Chen, Y. Yao, B. Liu, J. Song, G. Pastel, L. Hu, Hierarchically porous, ultrathick, "breathable" wood-derived cathode for lithium-oxygen batteries, Adv. Energy Mater. 8 (2018) 1600377, , https://doi.org/10.1002/aenm.201701203.

[41] X. Qian, X. Ren, D. Yue, Y. Zhu, Y. Han, Z. Bian, Y. Zhao, Mesoporous TiO$_2$ films coated on carbon foam based on waste polyurethane for enhanced photocatalytic oxidation of VOCs, Appl. Catal. B: Environ. 212 (2017) 1–6, https://doi.org/10.1016/j.apcatb.2017.04.059.

[42] Z. Wu, W. Li, P.A. Webley, D. Zhao, General and controllable synthesis of novel mesoporous magnetic iron oxide@carbon encapsulates for efficient arsenic removal, Adv. Mater. 24 (2012) 485–491, https://doi.org/10.1002/adma.201103789.

[43] X. Chang, B. Liu, H. Xia, R. Amin, High catalytic activity and stability of Ni/Ce$_x$Zr$_{1-x}$O$_2$/MSU-H for CH$_4$/CO$_2$ reforming reaction, Appl. Surf. Sci. 442 (2018) 342–351, https://doi.org/10.1016/j.apsusc.2018.02.068.

[44] H. Xia, B. Liu, Q. Li, Z. Huang, A.S.C. Cheung, High capacity Mn-Fe-Mo/FSM-16 sorbents in hot coal gas desulfurization and mechanism of elemental sulfur formation, Appl. Catal. B: Environ. 200 (2017) 552–565, https://doi.org/10.1016/j.apcatb.2016.07.053.

[45] M. Xing, B. Qiu, B. Du, Q. Zhu, L. Wang, J. Zhang, Spatially separated CdS shells exposed with reduction surfaces for enhancing photocatalytic hydrogen evolution, Adv. Funct. Mater. (2017) 1702624, https://doi.org/10.1002/adfm.201702624.

[46] D. Du, W. Shi, L. Wang, J. Zhang, Yolk-shell structured Fe$_3$O$_4$@void@TiO$_2$ as a photo-Fenton-like catalyst for the extremely efficient elimination of tetracycline, Appl. Catal. B: Environ. 200 (2017) 484–492, https://doi.org/10.1016/j.apcatb.2016.07.043.

[47] F. Raziq, L. Sun, Y. Wang, X. Zhang, M. Humayun, S. Ali, L. Bai, Y. Qu, H. Yu, L. Jing, Synthesis of large surface-area g-C$_3$N$_4$ comodified with MnOx and Au-TiO$_2$ as efficient visible-light photocatalysts for fuel production, Adv. Energy Mater. (2017) 1701580, https://doi.org/10.1002/aenm.201701580.

[48] A.E. Harvey, J.A. Smart, E.S. Amis, Simultaneous spectrophotometric determination of iron(II) and total iron with 1,10-phenanthroline, Anal. Chem. 27 (1955) 26–29, https://doi.org/10.1021/ac60097a009.

[49] T. Xu, R. Zhu, G. Zhu, J. Zhu, X. Liang, Y. Zhu, H. He, Mechanisms for the enhanced photo-Fenton activity of ferrihydrite modified with BiVO$_4$ at neutral pH, Appl. Catal. B: Environ. 212 (2017) 50–58, https://doi.org/10.1016/j.apcatb.2017.04.064.

[50] S.W.J. Boatright, G.G. Garrett, The effect of microstructure and stress state on the fracture behaviour of wood, J. Mater. Sci. 18 (1983) 2181–2199, https://doi.org/10.1007/BF00555013.

[51] Y. Teng, X.D. Wang, J.F. Liao, W.G. Li, H.Y. Chen, Y.J. Dong, D.B. Kuang, Atomically thin defect-rich Fe-Mn-O hybrid nanosheets as high efficient electrocatalyst for water oxidation, Adv. Funct. Mater. 28 (2018) 1802463, , https://doi.org/10.1002/adfm.201802463.

[52] D. Guo, X. Yu, W. Shi, Y. Luo, Q. Li, T. Wang, Facile synthesis of well-ordered manganese oxide nanosheet arrays on carbon cloth for high-performance supercapacitors, J. Mater. Chem. A 2 (2014) 8833–8838, https://doi.org/10.1039/c4ta01238k.

[53] P. Xiao, X. Ge, H. Wang, Z. Liu, A. Fisher, X. Wang, Novel molybdenum carbide-tungsten carbide composite nanowires and their electrochemical activation for efficient and stable hydrogen evolution, Adv. Funct. Mater. 25 (2015) 1520–1526, https://doi.org/10.1002/adfm.201403633.

[54] J. Wang, J. Li, C. Jiang, P. Zhou, P. Zhang, J. Yu, The effect of manganese vacancy in birnessite-type MnO$_2$ on room-temperature oxidation of formaldehyde in air, Appl. Catal. B: Environ. 204 (2017) 147–155, https://doi.org/10.1016/j.apcatb.2016.11.036.

[55] B. Zhang, L. Wang, Y. Zhang, Y. Ding, Y. Bi, Ultrathin FeOOH nanolayers with abundant oxygen vacancies on BiVO$_4$ photoanodes for efficient water oxidation, Angew. Chem. Int. Ed. 57 (2018) 2248–2252, https://doi.org/10.1002/anie.201712499.

[56] J. Bao, X. Zhang, B. Fan, J. Zhang, M. Zhou, W. Yang, X. Hu, H. Wang, B. Pan, Y. Xie, Ultrathin spinel-structured nanosheets rich in oxygen deficiencies for enhanced electrocatalytic water oxidation, Angew. Chem. Int. Ed. 54 (2015) 7399–7404, https://doi.org/10.1002/anie.201502226.

[57] N. Feng, J. Meng, Y. Wu, C. Chen, L. Wang, L. Gao, H. Wan, G. Guan, KNO$_3$ supported on three-dimensionally ordered macroporous La$_{0.8}$Ce$_{0.2}$Mn$_{1-x}$Fe$_x$O$_3$ for soot removal, Catal. Sci. Technol. 6 (2016) 2930–2941, https://doi.org/10.1039/C5CY02025E.

[58] W. Yang, R. Zhang, B. Chen, D. Duprez, S. Royer, New aspects on the mechanism of C$_3$H$_6$ selective catalytic reduction of NO in the presence of O$_2$ over LaFe$_{1-x}$(Cu, Pd)$_x$O$_{3-\delta}$ perovskites, Environ. Sci. Technol. 46 (2012) 11280–11288, https://doi.org/10.1021/es302240m.

[59] X. Tang, J. Li, L. Sun, J. Hao, Origination of N$_2$O from NO reduction by NH$_3$ over β-MnO$_2$ and α-Mn$_2$O$_3$, Appl. Catal. B: Environ. 99 (2010) 156–162, https://doi.org/10.1016/j.apcatb.2010.06.012.

[60] P.J. Gellings, H.J.M. Bouwmeester, Solid state aspects of oxidation catalysis, Catal. Today 58 (2000) 1–53, https://doi.org/10.1016/S0920-5861(00)00240-6.

[61] Z. Wan, J. Wang, Degradation of sulfamethazine using Fe$_3$O$_4$-Mn$_3$O$_4$/reduced graphene oxide hybrid as Fenton-like catalyst, J. Hazard. Mater. 324 (2017) 653–664, https://doi.org/10.1016/j.jhazmat.2016.11.039.

[62] C. Su, X. Duan, J. Miao, Y. Zhong, W. Zhou, S. Wang, Z. Shao, Mixed conducting perovskite materials as superior catalysts for fast aqueous-phase advanced oxidation: a mechanistic study, ACS Catal. 7 (2017) 388–397, https://doi.org/10.1021/acscatal.6b02303.